Engineering Structures 306 (2024) 117782

Contents lists available at ScienceDirect

Engineering Structures

journal homepage: www.elsevier.com/locate/engstruct

A novel design of multifunctional offshore floating platform structure based on topology optimization

Nouman Saeed [a], Jingliang Gong [a], Yuejia Wan [a], Kai Long [c], Ayesha Saeed [c], Liu Mei [a], Chen Xiong [a], Wujian Long [a], Haijun Zhou [a,b], Lixiao Li [a,b,*]

[a] College of Civil and Transportation Engineering, Shenzhen University, Shenzhen 518060, China
[b] Shenzhen Key Laboratory of Structure Safety and Health Monitoring of Marine Infrastructures, College of Civil and Transportation Engineering, Shenzhen University, Shenzhen, China
[c] State Key Laboratory of Alternate Electrical Power System with Renewable Energy Sources, North China Electric Power University, Beijing 102206, China

ARTICLE INFO

Keywords:
Topology optimization
Offshore wind turbine
Multifunctional platform structure
Structural analysis

ABSTRACT

Floating platforms are an economical option for offshore energy harvesting in deep water sea. Lightweight design and structural stability are most important concerns in the design of floating foundations under the premise of ensuring load-bearing capacity. Topology optimization has proven to be a successful method for determining the optimal material distribution with the desired stiffness, strength, and robustness of the subjected design structure. In this paper, a novel lightweight multifunctional offshore floating platform design is proposed utilizing the density-based topology optimization method for the combined utilization of wind-solar-wave energy. Firstly, based on the extreme sea conditions in the South China Sea, the minimum compliance subject to the prescribed volume percentage is formulated and an innovative platform structure is carried out by interoperating the variable density method in the ANSYS AQWA module. Secondly, the optimized floating platform structure was strength-checked based on the maximum von Mises stresses under extreme loading conditions specified in the DNV code. The total mass of the novel optimized structure is 40.82% of the primary structure. Moreover, the platform stiffness and durability have been significantly enhanced.

1. Introduction

As fossil energy sources cause severe pollution to the environment, the development and utilization of green and clean renewable energy sources is an important tool for combating climate change and realizing carbon and emission reductions [1]. Wind energy is recognized as a primary source among renewable energy sources and it has grown significantly in recent decades in both onshore and offshore industries (Global Wind Energy Council, 2019) [2,3]. Compared with the development of onshore wind energy, offshore wind energy has various advantages, such as a more stable wind resource, a larger geographic area that can be exploited, and less visual and noise interference, so it has a bright prospect for development and utilization [4]. With the development of offshore energy to the deep sea (water depth over 60 m), the traditional fixed foundation is faced with technical challenges such as the use of more materials, high construction costs, construction difficulties, etc. Therefore, the floating foundation form is an attractive choice for deep-sea wind energy development. The tension leg platform (TLP), barge, spar buoy, and semi-submersible are the four most frequent types of floating offshore wind turbines (FOWTs) foundation [5]. Due to the six degrees of freedom (DOFs) of the platform, FOWTs are more susceptible to damage by wind and wave forces compared to fixed-bottom offshore turbines [6]. Therefore, platform stabilization is a key consideration in substructure and controller design. Lack of control authority on the platform DOFs is a prevalent problem across various substructure systems [7].

Cost reduction is key to the development of floating wind turbines. The cost of floating wind turbines depends mainly on the characteristics of the floating infrastructure structure they use [8–10]. Floating wind turbine infrastructure design should take into account both cost issues and the impact of floating foundations on the operational stability of the overall power generation system [11,12]. The average levelized cost of FOWT energy can be attained via increasing annual energy production (AEP), minimizing the capital expenditures (CapEx), and decreasing operation and maintenance (O&M) expenses, all of which may be attained through the contributions of topology optimization (TO) based

* Corresponding author at: College of Civil and Transportation Engineering, Shenzhen University, Shenzhen 518060, China.
E-mail address: lilixiao@szu.edu.cn (L. Li).

https://doi.org/10.1016/j.engstruct.2024.117782
Received 10 September 2023; Received in revised form 22 December 2023; Accepted 26 February 2024
Available online 12 March 2024
0141-0296/© 2024 Elsevier Ltd. All rights reserved.

innovative floating platform designs [13]. In structural optimization, topology optimization (TO) is a lightweight design method that can identify the optimal material distribution within a specific design domain subject to a particular set of loads and boundary conditions [14–19]. Bendsoe and Kikuchi were the first to introduce the TO approach in 1988 [20]. Later on, numerous TO approaches have been implemented [21–26], leading to tremendous advancements such as aircraft and aerospace [27,28], automobile [29], compliant mechanisms [30], battery [31] industries, and metamaterial designs [32]. Reviews on certain methods are provided by Sigmond et al. [33] for the variable density method. Despite the widespread recognition of the vital role of structural optimization, little attention has been placed on developing OWT foundations or subsystems using the TO paradigm [34–36]. Currently, floating platforms often rely on early empirical design-based prototypes, which have certain material redundancy. Therefore, optimizing the platform structure with the goal of weight reduction will bring economic benefits. Zhang et al. (2022) [37] were the first individuals to recognize the relevance of the topological features in mechanical behavior and suggested an in-depth review of the OWT jacket platform structure. Tian et al. (2022a, 2022b) [38,39] implemented the combined size, shape, and topology optimization approaches to obtain a lightweight design for jacket structures. Karimi et al. [40,41] executed a multi-objective optimization approach aiming to minimize the construction cost of a 5 MW FOWT. Yang et al. (2015) [42] proposed a topology optimization-based design approach for improving the OWT tripod platform while meeting dynamic response requirements. Gentils et al. (2017) [43] suggested an integrated optimization approach for OWT support structures using the genetic algorithm and parametric finite element (FE) analysis by optimizing the outer diameter and thickness simultaneously. Motlagh et al. (2021) [44] introduced a genetic algorithm that exercised design factors including the members' outer diameter and thickness to optimized the jacket platform structure. Song et al. [45] implemented a topology optimization approach to carry out a conceptual structural optimized design for the 10 MW FOWTs hybrid platform and obtained the bridge-like floating platform structure containing the impact of marine environmental loads and functional loads. Tian et al. [46] carried out variable density-based topology optimization for the jacket structure of the wind turbine. Compared with the original structure, the newly designed structure reduced the total weight by 13.7% and the maximum stress by 46.31%, increasing the bearing capacity of the structure. Structure optimization is an essential step during the design process for massive multifunctional floating offshore platforms.

To the best of the authors' knowledge, in-depth application of TO on the multifunctional floating platform structure has been systematically conducted that can effectively reduce the weight and can further improve the platform configuration design robustness, but the relevant research is still in the initial stage. The fundamental theme of this work focuses on maximizing the stiffness to address the challenges of poor stability and minimizes the cost of the proposed multifunctional floating optimized platform by utilizing the density-based topology optimized approach and proposed optimized platform incorporates various ocean energy power generation mechanisms, such as wind, solar, and wave energy equipment that all are combined installed on a single platform to increase the offshore green energy production. The following sections comprise the paper: Section 2 describes the layout of the proposed platform and the parameters of the reference power generation energy components that are installed at the proposed platform. Section 3 describes how to apply the TO technique to the proposed multifunctional platform structure design utilizing the commercial software ANSYS AQWA according to the extreme conditions of the South China Sea. In Section 4, a novel optimized platform structure is restructured. Section 5 describes the static structural analysis and checks the strength verification of the optimized platform by applying the static various load cases that meet the design requirements of DNV specifications. Subsequently, the main findings of this study are presented in the conclusion Section 6.

2. Layout and parameters configuration of the multifunctional platform

The suggested design of the multifunctional floating platform integrates the reference three wind turbines, wave energy power generation devices and solar panels. The preliminary design configuration of the hexagonal floating platform is depicted in the following Fig. 1. Based on the analysis of wake flow interference effects of wind turbines and the size characteristics of conical oscillating float, the side length of the proposed platform is set to be 215 m that carries wave energy devices, a large deck is at the top of the platform where photovoltaic panels will be installed and in detail information is given in Table 1.

2.1. Wind turbine parameters and layout analysis

Three DTU 10 MW OWTs as the reference models are equipped together at three corner columns of a single proposed multifunctional floating optimized platform and relevant key parameters are summarized in following Table 2.

The spacing of multiple wind turbines at the same platform is subjected to various constraints such as, platform cost, towing installation, the operating sea area and other aspects [48]. It is impossible to determine the spacing of wind turbines by fully considering the wake effect like land wind farms. The spacing of the turbines needs to take into account the structure of the floating platform, the effect of wake, the cost of construction, etc. Therefore, it is recommended that the spacing of wind turbines in the same wind direction should be maintained at a distance of about two times the diameter of the wind turbine blades [49, 50].

In this study, the Jensen wake model is utilized to analyze the shielding effect of upstream wind turbine on downstream wind turbine. It is assumed that the initial range of the wake influence is the diameter of the wind turbine, and the wake growth rate is linear, and the wind speed is eventually distributed in the transverse profile of the wake. The schematic diagram of the Jensen wake model is shown in Fig. 2.where v_1 is the wind speed from the upstream wind turbine, R_r is the wind turbine blade length,v_x is the wind speed at the wake, x is the vertical distance between upstream and downstream wind turbines, R_w is the wake diameter, and K is the wake expansion coefficient, usually $K \approx 0.1$[51].

Three wind turbines will be symmetrically arranged on the three corner columns of the hexagonal floating platform at 120° intervals, spacing between wind turbines is twice the diameter of the wind turbine rotor. Consider the influence of upstream wind turbines on the downstream wind turbines in the range of 0°∼60°, and take 0°, 30° and 60° as the typical wind directions and the wake expansion coefficient K take 0.07. The schematic diagram of wake occlusion under different wind directions is shown in Fig. 3.

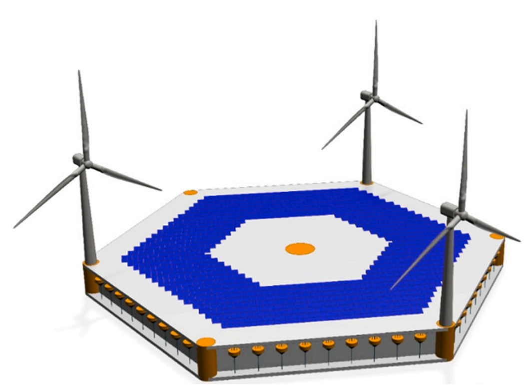

Fig. 1. Functional layout of Energy Floating Platform.

Table 1
Main Dimension Parameters of Energy Floating Island Platform.

Name	Value
Platform side length	215 m
Platform draft	22 m
Platform depth	33 m
Outer column diameter	16 m
Central column diameter	30 m
Water depth	200 m
Deck height	3 m
Number of columns	7
Float diameter	16 m
Float height	33 m
Distance from the center of the float	206 m
Center of gravity of platform (x, y, z)	-5.50 m

Table 2
Reference DTU 10 MW OWTs key parameters [47].

Name	Value
Rated Power	10 MW
Rotor diameter	178.3 m
Number of Blades	3
Cut-in wind speed	4 m/s
Rated wind speed	11.4 m/s
Cut out wind speed	25 m/s
Hub diameter	5.6 m
Tower Height	115.63 m
Tower diameter at upper end	5.32 m
Tower diameter at lower end	11.5 m
Rotor weight	227.962 t
Engine weight	446.036 t
Tower weight	628.442 t
Wind turbine weight	1302.44 t
Total wind turbines weight	3927 t

2.2. Parameters of wave energy power generation device

According to different power generation principles, wave energy power generation devices can be categorized into point absorbers, oscillating water columns, attenuators, and oscillating wave surge converters [51,52]. Considering the stability of captured energy and the influence of the operating environment, the conical point absorber wave energy generation device is adopted in this paper, with a single float capturing power of about 96 kW. The working principle of an oscillating float is mainly to collect wave energy through its movements at/near the water's surface and then convert it into hydraulic or mechanical energy. The main factors affecting the hydrodynamic performance of oscillating point absorber are float size, shape, draft depth etc. The natural frequency of a cone is greater than that of a hemisphere and a cylinder, which can capture higher frequency waves [53,54]. The hexagonal platform is arranged with 9 floats on one side, with a spacing of 20 m b/w the floats. Referring to the conversion rate of the Wanshan power generation device of Guangzhou Energy Research Institute (about 85–90%) [55], the power generation capacity of the wave energy power generation device of the total 54 devices is about 4.4 MW. The specific parameters of the oscillating floats are shown in Table 3.

2.3. Parameters of solar photovoltaic power generation device

To capture solar radiation energy and transform it into electrical energy, photovoltaic power production mostly requires solar cells, and semiconductor electronic components [56]. The conversion rate of photovoltaic technology has further grown with advancements in the field, and the cost is also steadily declining. Solar cells can be divided into silicon solar cells, multi-compound thin-film solar cells, and polymer solar cells [57]. Silicon solar cells convert solar radiation into energy with a high conversion rate of 15–20% and stable performance. Comprehensively, considering all factors, the 345WP polycrystalline silicon photovoltaic module is adopted as a reference model [58]. The output power of each 1 m^2 of photovoltaic panels is about 170 W, the total captured area of photovoltaic panels is 67058.6 m^2, and the anticipated power generation may be 11.4 MW. The main parameters are shown in Table 4.

3. Topology optimization of the floating platform structure

3.1. Topology Optimization

The topology optimization approach is utilized to achieve the optimal material distribution and the optimal structure with the desired maximum stiffness, strength and robustness of the subjected design structure under multiple loads and boundary conditions. TO is applied to achieve the durable and lightweight design structure of the proposed multifunctional floating platform under the action of multiple wind turbines, solar, wave energy power generation devices, mooring lines loads, and working sea conditions are as shown in Fig. 4. In this study, the working condition of the floating platform is selected as the extreme sea state of the South China Sea under the action of wind, wave and current with the return periods of fifty years, which means that the wind speed of 39.2 m/s at the height of 10 m and 52.6 m/s at the height of the

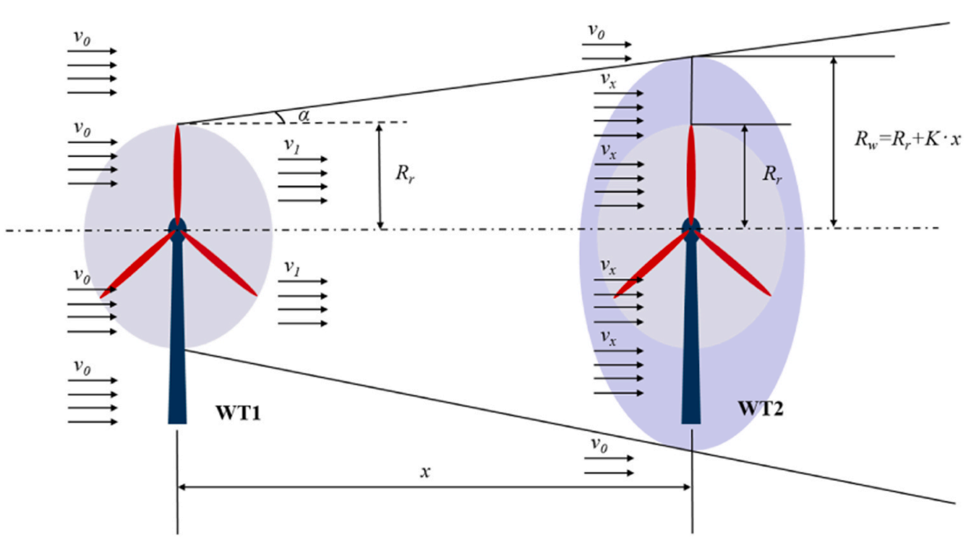

Fig. 2. Schematic diagram of Jensen wake model.

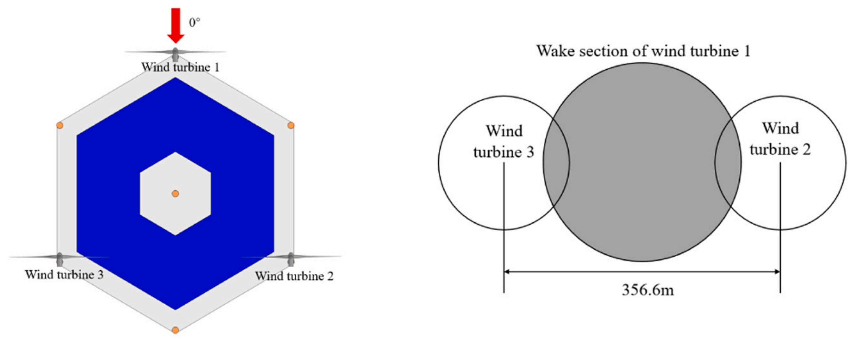

(a) 0° wind direction

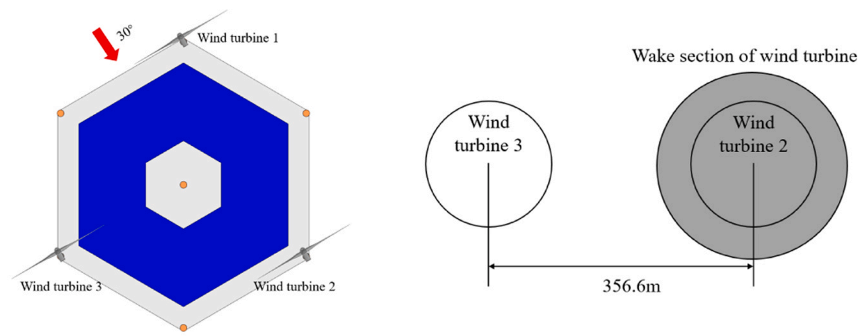

(b) 30° wind direction

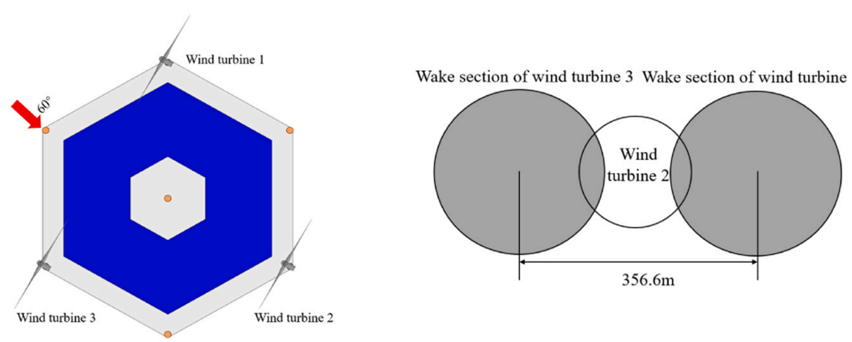

(c) 60° wind direction

Fig. 3. Schematic diagram of wake occlusion under different wind directions.

Table 3
Main parameters of oscillating float.

Name	Value
Cone bottom angle	90°
Draft	2 m
Radius	5 m
Distance between the floats	20 m
Single float mass	134 t
Number of floats on each side	9
Total number of floats	54
Center of gravity	(0,0,−1.20)m
Total weight	7236 t

Table 4
345 Wp Polycrystalline Silicon PV Module.

Name	Value
Maximum output	345 W
Open circuit voltage	46.4 V
Short circuit current	9.62 A
Working voltage	37.7 V
Working current	9.15 A
Conversion rate	17%
Output power difference	0-5 W
Operating temperature	-40-80 C^0
Overall dimensions (l,w,h)	2024 * 1004 * 35 mm
Weight	22 kg
Center of gravity	(0,0,11.02)m
Total Weight	2.84×10^6 t

hub, and the parameters of the wave load condition are selected as the significant wave height of 12.5 m, a period of 13.7 s, and the surface current speed of 1.4 m/s. Due to the maximum area of wind and wave in the y-direction, the exerted pressure subjected to wind and wave influence at 90° of the floating platform. The gravity load of the photovoltaic panel and wave energy power generation devices in the internal load of the platform is far less than the wind turbine load, mooring loads and wave load.

3.1.1. *Wind load of wind turbines*

The offshore floating platform not only bears environmental loads

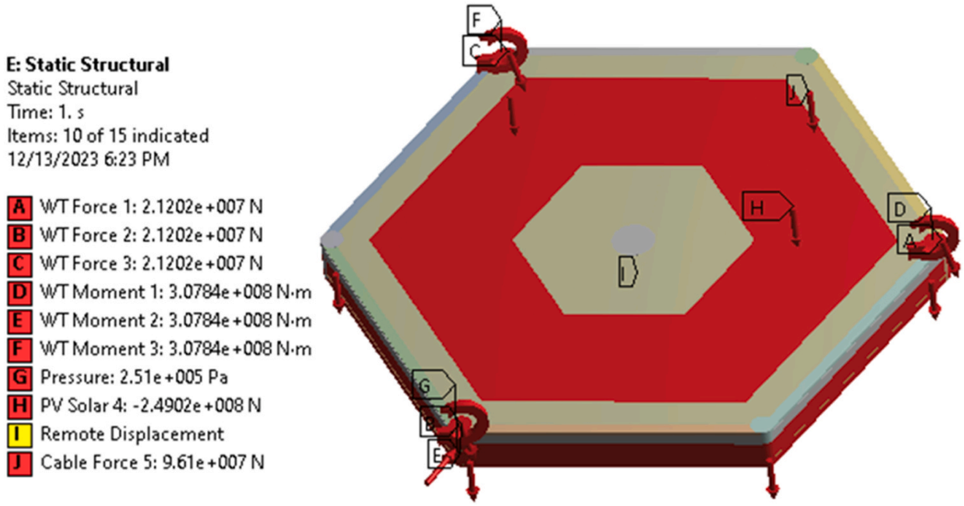

Fig. 4. Forces at platform.

but is also subjected to the loads transmitted from the upper wind turbines to the top of the platform, including the turbines' weight, shear and bending moments. The loads of the three DTU 10 MW wind turbines on the upper part of the platform was simulated using the open FAST software developed by the Renewable Energy Laboratory (NREL). The open FAST software simulated 700 s of load data and intercepts 100–700 s, and the statistically extreme values of the load at the bottom of the tower are shown in Table 5.

3.1.2. Mooring system and wave loads

In this study, ANSYS AQWA is used to calculate the mooring load and wave load of the platform. Since the platform subsequently needs to optimize the internal arrangement of the solid hexagonal platform model, to obtain the mooring load and wave load of the platform, the outer surface model of the hexagonal body is established in AQWA as a simplified model for the floating body motion analysis. Six corners of the platform are used as fairleads for mooring arrangements. Each fairlead is connected with four catenary mooring lines. The incorporated angle of mooring lines in the same fairlead is 20°, and the length of mooring lines is 1020 m, as shown in Fig. 5.

The time domain calculation step is 0.2 s, and the simulation time is 3 h. Due to the symmetry of the platform, the mooring tension of node 5 is the same as that of node 6, with the maximum total mooring tension of node 6. The mooring tension time history curves of the four mooring lines at node 5 are shown in Fig. 6. The maximum mooring tensions of mooring lines # 5–1, # 5–2, # 5–3, and # 5–4 are 2.09×10^7 N, 1.85×10^7 N, 1.34×10^7 N, 8.63×10^6 N, with a maximum total mooring tension of 6.14×10^7 N.

The wave load is calculated by sharing the Geometry in the Hydrodynamic Diffusion module of ANSYS workbench with the Static Structural module, and the wave surface pressure load is shown in Fig. 7. The maximum wave load surface pressure is about 2.51×10^5 Pa, select the wave load value and applied it onto the outer surface of the model below the cutting surface.

Table 5
Extreme value statistics of tower bottom load.

Name	Simulated result
X-direction load/kN	4152
Y-direction load/kN	690.5
Z-direction load/kN	-20780
Bending moment at X /kN·m	-65010
Bending moment at Y /kN·m	300800
Bending moment at Z /kN·m	-7552

The flowchart of the proposed multifunctional floating platform embedded with the TO of this paper is shown in the following Fig. 8.

3.2. Topology optimization on the proposed multifunctional platform design

In this section, TO will be applied to achieve a durable and lightweight design. As the proposed design domain of the floating offshore platform structure is depicted in Fig. 9, the platform model has participated in two regions. The exclusion region is reserved by the deck plane for the photovoltaic panel and the lower beam supports the oscillating float power generation devices and the remaining areas are devoted to topology optimization. The platform model used ultra-high strength steel EH36, the material density is 7850 kg/m^3, the elastic modulus is 2.1×10^{11} Pa, Poisson's ratio is 0.3, and the yield stress is 355 MPa.

The purpose of topology optimization is to meet the best material distribution for the proposed model through the given design domain, constraints, and force transmission path. Considering the maximization of stiffness in static problem. Minimize compliance may be expressed as,

$$l(u) = \int_{\Omega} Fud\Omega \int_{\Gamma_t} Tuds + \sum\nolimits_i^n F_i u_i \tag{1}$$

where external force and displacement vectors are denoted by F and u; T is the boundary distributed force. The expression of the topology optimization problem can be expressed as,

$$\begin{aligned} &\min \quad c = l(u(x)) \\ &s.t. \quad \sum_{j=1}^{n} x_j v_j \le V_0 \\ &0 < x_{\min} \le x_j \le 1 \quad j = 1, 2, 3, ., n \end{aligned} \tag{2}$$

Here, the objective function l concerning minimizing compliance; $x$is the density design variable vector; $v_j$is the solid structural volume of the element j, and $V_0$is the volume of the design domain. The variable density method known as the pseudo-density material, takes the hypothetical material relative density as the design variable for optimization design iteration, and the relative density ranges from 0 to 1 respectively.

$$X_i(x) = \begin{cases} 1 & x \in \Omega_s \\ 0 & x \in \Omega/\Omega_s \end{cases} \tag{3}$$

Density and elasticity matrix expressions are:

$$\begin{aligned} p(x) &= X_i(x)\rho^o \\ E(x) &= X_i(x)E^o \end{aligned} \tag{4}$$

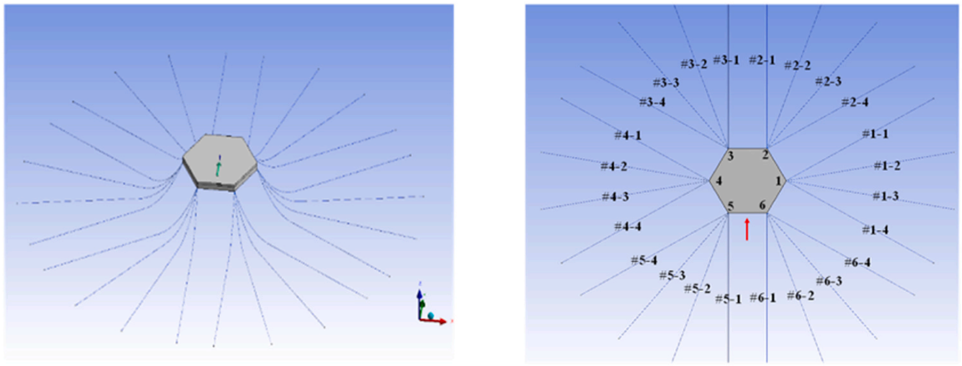

Fig. 5. Platform mooring arrangement.

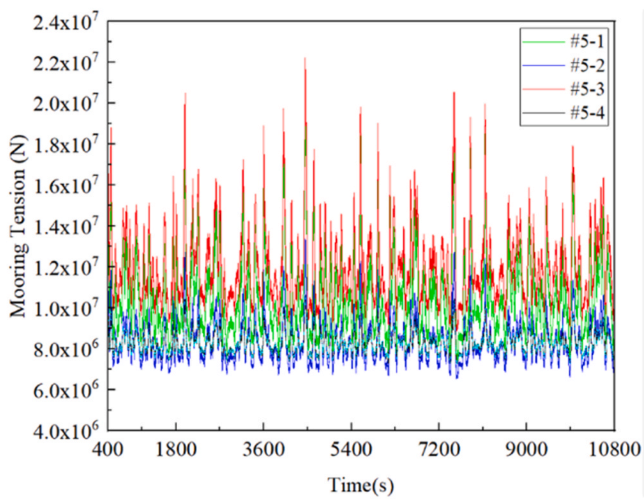

Fig. 6. Time history curve of mooring tension at node 5.

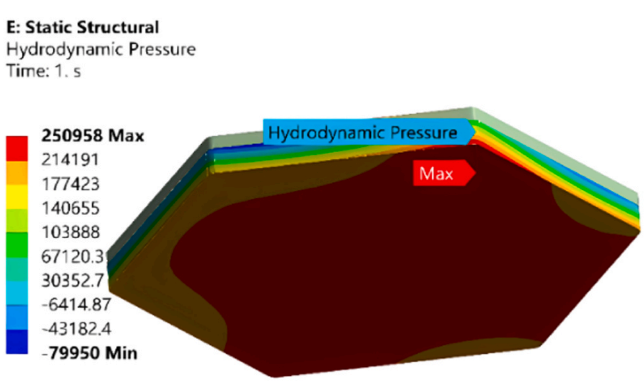

Fig. 7. Wave load surface pressure (T = 13.7 s, Hs=12.5 m, wave incidence angle 90°).

where, ρ^{o} and E^{o} represent the density and elasticity matrix respectively.

3.2.1. Modified solid isotropic material with penalization (SIMP)

In the optimization process, many intermediate densities between 0 and 1 will be generated. In reality, this material does not exist. A critical aspect of the density-based method is the selection of an appropriate function and penalization technique to express the physical quantities. Here modified SIMP is employed to interpolate Young's modulus function of these intermediate densities. It operates on a fixed domain of the FE to identify each element.

$$E(x_j) = \left[\frac{x_{\min} - x_i^p}{1 - x_{\min}^p}\left(1 - x_j^p\right) + x_j^p\right]E^1 \quad \left(0 < x_{\min} \leq x_j \leq 1\right) \tag{5}$$

where, x_j is the relative density, p is the penalty factor, E^1 is Young's modulus of the solid material.

3.2.2. Topology-optimized platform structure

TO process is evaluated utilizing the commercial engineering software Ansys to consider the wind turbines, oscillating float devices, solar panels, gravity, mooring lines, and aero-hydrodynamic ultimate loads scenarios. Fig. 9 shows the design domain of the proposed platform.

In the TO setting, the proposed model is divided into 177720 finite elements by using a hexahedral mesh with each element size of 3 m. Fig. 10 depicts the topology optimized layout of the platform model with different cell densities after 55 iterations and taking 31 h calculation time. The cell density threshold range of 0–0.4 is to be removed, while the range of 0.4–0.6 is the transition zone, and if it exceeds 0.6, it will be retained. The following results show that the materials around the central column in the platform are distributed in a regular hexagon. The force transmission path between the central and the outer columns is mainly transmitted through the three transverse braces and the bottom plate extending from the middle hexagon.

4. Reconstruct the topology optimized proposed platform

The model after topology optimization is often not a regular and easy-to-manufacturing configuration, so it is necessary to redesign the model manually according to the results of topology optimization. The truss structure is used to model the results of the design area, and the connections between the columns and the lower beam. Inner and outer hexagonal trusses are used as the main supports in the middle hexagonal coated by a light blue zone, and a diagonal web member is used to increase the internal stiffness. Three longitudinal braces are designed in the orange zone as the connection between the bottom of the outer column, lower beam and the middle blue zone, as well as two transverse braces are added in the middle to replace the gray density unit at the bottom. At the same time, vertical braces are added to connect the top deck, diagonal braces are designed between the vertical brace and the transverse brace to increase the stiffness of the bar connection. The diameter of transverse and vertical bracing is 5 m, and the diameter of slant support is 4 m respectively. The preliminary model of the topology optimization area of the floating platform is shown in Fig. 11.

4.1. Deck

The main function of the deck is to carry the upper solar photovoltaic panels and other supporting equipment. The side length of the hexagonal deck is about 215 m and the height is 3 m with 100 mm thickness. Hexagonal transverse ribs are arranged at an interval of 6 m along the

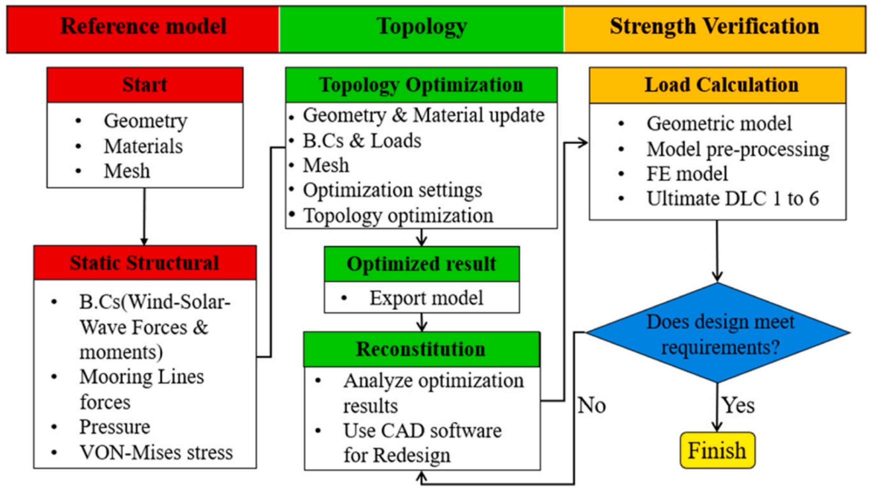

Fig. 8. Flowchart of the proposed multifunctional floating platform embedded with TO.

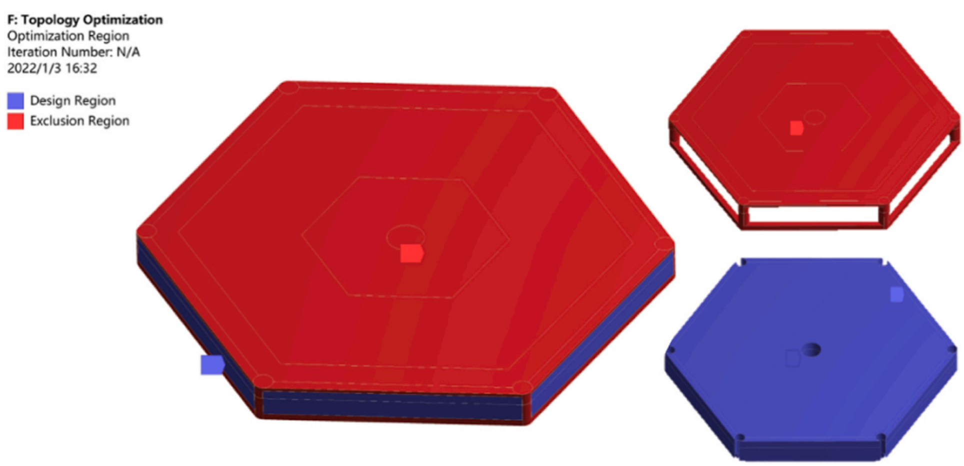

Fig. 9. Design domain of the proposed platform.

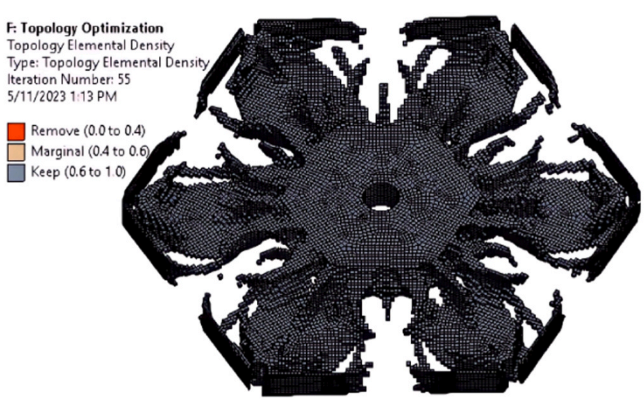

Fig. 10. Material density distribution.

circumferential direction inside, and longitudinal ribs are arranged at an interval of 5° along the circumferential direction of the central column. Transverse ribs near the outer columns are locally densified based on the distribution of the vertical ribs inside the outer column. Here, longitudinal ribs are connected with the internal longitudinal ribs, and triangular diagonal support is added at the corner connection of the longitudinal ribs connecting the central and outer columns. The internal structure of the deck is shown in Fig. 12.

4.2. *Outer column*

The columns are mainly used to support the upper part of the platform deck, and can also be arranged in the cabin for ballast water. The floating platform model is equipped with a 6 m ballast tank at the lower part of the outer column to achieve the effect of an offshore platform's heave by adjusting the height of the water wave. The upper section of the outer column has a diameter of 16 m, the lower ballast tank has a diameter of 22 m, the outer wall thickness is 100 mm, and the inner rib plate has a thickness of 30 mm. Longitudinal ribs are arranged vertically at 30° intervals along the circumference, and the spacing between circumferential ribs is 6 m, 9 m and 9 m from top to bottom respectively. In addition, reinforcement materials are placed along the outer surface, steel ribs are positioned vertically at 10° intervals around the circumference, flat steel is positioned internally at 10° intervals on the upper and lower surfaces of the vertical tank, and flat steel is positioned at 2 m intervals as reinforcement material. The internal structure of the outer column is shown in Fig. 13.

4.3. *Middle column*

The internal structure layout of the central column is shown in Fig. 14. The diameter of the central column is 30 m, the outer wall thickness is 100 mm, and the thickness of the inner rib plate is 30 mm. Vertical longitudinal ribs are arranged at 30°, and the spacing between

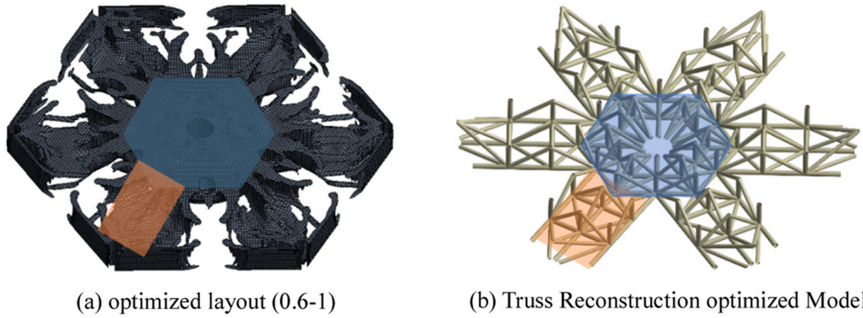

Fig. 11. Comparison of topology reconstruction models in the design area.

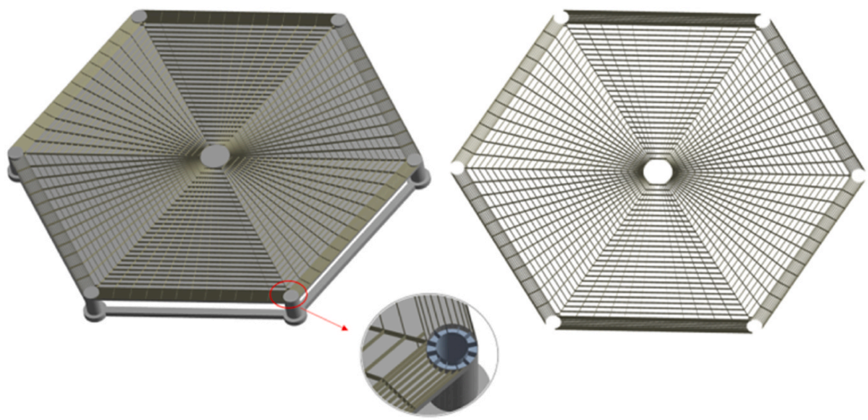

Fig. 12. Deck internal structure.

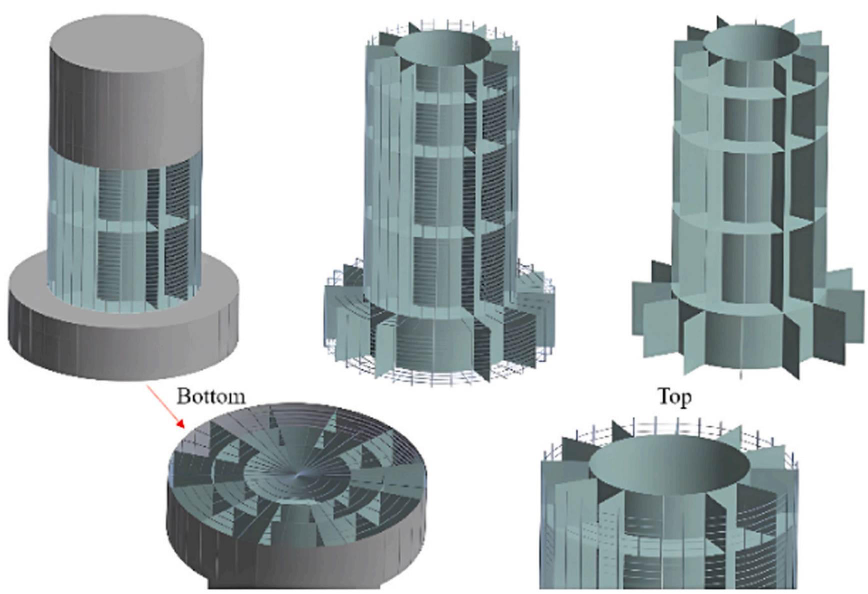

Fig. 13. Outer Column structure.

the circumferential rib plates is 6 m, 9 m, 9 m, and 3 m from top to bottom. Arrange angle steel 10° along the outer surface of the column, and arrange circumferential flat steel 500 mm vertically as reinforcement material. The bottom surface radiates outward along the center of the circle with circular flat steel 3 m.

4.4. Lower beam

The main role of the lower beam is to carry the conical point absorber wave energy generation devices and interconnect the ballast tank under the adjacent outer column, cross section of the beam is 8 × 6 m and the rectangular section with an outer wall thickness is 100 mm. A transverse rib is 5 m along the longitudinal direction, a longitudinal rib is arranged in the longitudinal centerline, and the thickness of the rib plates is

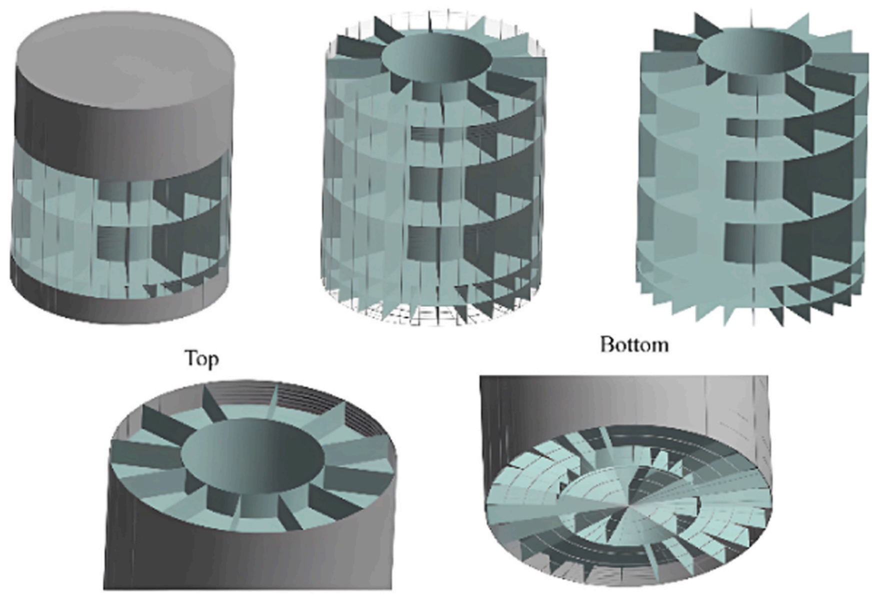

Fig. 14. Internal structure of the central column.

30 mm. The internal structure is shown in Fig. 15.

Table 6 shows the dimensional parameters of the optimized platform.

5. Structural strength and safety analysis of the optimized floating platform

5.1. Strength verification method for the multifunctional floating platforms

The design load of marine infrastructure is relatively complex, the accurate estimation and assessment of the load magnitude and action mode are of great significance for evaluating the strength of large platforms. To verify the structural strength of the optimized platform, a strength verification analysis was conducted on the reconstructed platform model. The loads acting on the floating platform structure include permanent loads, variable live loads, environmental loads and incidental loads, etc. The DNV-OS-J101 standard [59] stipulates that the design load condition of the floating platform structure should consider the combination of the ultimate limit state, fatigue limit state, accidental limit state and serviceability limit state. Focuses on the loads and bending moments in the x, y, and z directions transmitted by the wind turbines, wave energy generation devices, and solar photovoltaic panels. The design draft of the model is 22 m, and the water injection height for the six degrees of freedom compartments and the lower portion of the central column is 4 m. The hydrostatic pressure is computed. The specific load conditions are shown in Table 7.

Table 6
Dimensional parameters of the optimized platform.

Name Specification	Size unit
Column diameter	16 m
Column height	27 m
Heave chamber diameter	22 m
Heave chamber height	6 m
Middle column diameter	30 m
Middle column Height	30 m
Cross brace diameter	5 m
Slant diameter	4 m
Water depth	200 m
Design water	22 m
Platform mass	297818 tons
Drainage capacity	313467 tons
Longitudinal ribs	30°

5.2. Calculation of wave load on the optimized platform

The calculation method of wave loads is mainly based on the design wave method to select the most severe conditions of typical wave conditions to obtain the design wave parameters such as meaningful wave height, period, wave direction angle, and phase of the corresponding wave spectrum. Common wave load calculation methods include the deterministic design wave method, stochastic design wave method, and long-term prediction method [60]. ANSYS AQWA is utilized to calculate the wave load acting on the platform exercising the deterministic design wave method, the hydro surface model of the platform is established since the internal structure and material properties of the platform will

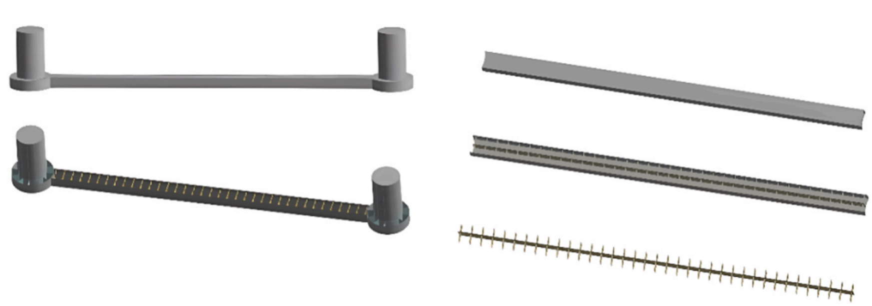

Fig. 15. Internal structure of Beam.

Table 7
Ultimate state operating conditions of bearing capacity.

LCs	Permanent Load	Environmental loads
LC1		External static water load+design wave 1
LC2	Internal static water load	External static water load+design wave 2
LC3	+Wind turbine load	External static water load+design wave 3
LC4	+Gravity of wave energy power generation equipment	External static water load+design wave 4
LC5	+Photovoltaic panel gravity	External static water load+design wave 5
LC6		External static water load+design wave 6

not affect the calculation results of the hydrodynamic performance of the model. The hydrodynamic model platform is established as shown in Fig. 16, with a total of 38447 model finite elements.

In combination with the DNV specification and the selection of key profiles of relevant offshore engineering examples [61,62], the platform mid transverse section *xoz* plane and mid-longitudinal section *yoz* plane are taken as key profiles, and the origin coordinates are the intersection points of the mid-transverse section, mid-longitudinal section, and hydroplane. To calculate the wave load in ANSYS AQWA, the wave incidence angle is set up from -180° to 180° with intervals of 15° and the wave period is set up from 4–18 s, with intervals of 0.5 s between 7–15 s and 1 s interval is set between other wave period ranges in the Hydrodynamic Diffraction module. However, the floating optimized platform model is symmetrical about the x and y axes, therefore we specifically choose the wave incidence angle from 0° to 90°, and the calculated hydrodynamic characteristics response of each profile are shown in Table 8. The Response Amplitude Operator (RAO) represents the response amplitude of the floating optimized platform structure to waves and the maximum response value is known as the response peak.

By comparing the maximum forces and moments in each section, three typical hydrodynamic characteristic parameters corresponding to the design wave parameters and acceleration were selected. A total of six design wave parameters were selected as the most dangerous operating condition control parameters, and the relevant parameters are shown in Table 9.

5.3. Analysis of strength verification results for the platform

Based on the obtained six design wave parameters, the corresponding wave loads on the platform were calculated using Hydrodynamic Diffraction. The wave loads were mapped to the outer surface of the platform using the ANSYS workbench. Calculate the Equivalent (von Mises) Stress cloud map of each component of the platform by combining other loads.

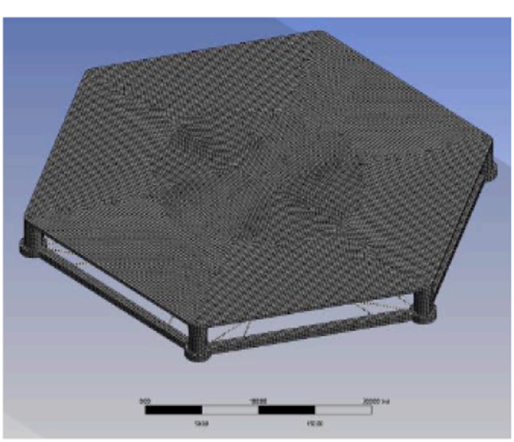

Fig. 16. Hydrodynamic platform model.

Table 8
Parametric statistics of hydrodynamic characteristics.

Hydrodynamic characteristic parameters	Period	Angle	Height	RAO	Response Peak
Axial force at mid-transverse	8 s	0^0	12.775 m	1.19E+ 07	7.62E+ 07
Transverse shear force at mid-transverse	11.5 s	90^0	17.300 m	1.83E+ 07	1.58E+ 08
Vertical shear force at mid-transverse	8.5 s	30^0	13.992 m	6.98E+ 06	4.89E+ 07
Longitudinal torque at mid transverse	7.5 s	90^0	11.561 m	9.37E+ 08	5.41E+ 09
Transverse bending moment at mid-transverse	10.5 s	45^0	15.998 m	8.47E+ 08	6.78E+ 09
Vertical bending moment of mid-transverse	8.5 s	0^0	13.993 m	1.85E+ 09	1.29E+ 10
Longitudinal shear force at mid-longitudinal	8 s	0^0	12.775 m	1.49E+ 07	9.54E+ 07
Axial force at mid-longitudinal	7.5 s	90^0	11.561 m	1.22E+ 07	7.06E+ 07
Vertical shear force at mid longitudinal	8.5 s	75^0	13.992 m	6.18E+ 06	4.32E+ 07
Longitudinal bending moment at mid-longitudinal	10.5 s	45^0	15.998 m	8.51E+ 08	6.81E+ 09
Transverse torque at mid longitudinal	8.5 s	30^0	13.993 m	8.36E+ 08	5.85E+ 09
Vertical bending moment at mid-longitudinal	8 s	45^0	12.776 m	1.37E+ 09	8.76E+ 09
Lateral acceleration	10.5 s	90^0	15.998 m	0.067	0.536
Longitudinal acceleration	10.5 s	30^0	15.998 m	0.058	0.465
Vertical acceleration	18 s	90°	17.300 m	0.048	0.418

Note: Peak response units of force, torque, and acceleration are N, Nm, and m/s^2.

From Fig. 17, it can be seen that the overall structure of the platform exhibits stress concentration in key areas where components are connected. Among them, the maximum equivalent stress 352.76 MPa occurs at the connection between the cross brace, slant support and the central column respectively.

The maximum equivalent stress 283.56 MPa occurs on the shell of the platform at the outer surface of the lower crossbeam, that is the intersection of the transverse brace and the lower crossbeam, as shown in Fig. 18. The stress on the lower crossbar is generally high and is mostly affected by wave power generation devices and wave loads. Furthermore, maximum equivalent stress areas appeared at the junction between the outer, central columns and the top plate, as well as at the connection between the vertical support and the bottom of the deck.

It can be seen from Fig. 19 that the maximum equivalent stress occurs at the corner of the cross brace and slant support that is connected to the lower part of the central column, and the maximum value is 181.57 MPa. The equivalent stress value of slant support near the center connected with the deck is about 160 MPa, and the equivalent stress of slant support connected with each outer column can reach 120 MPa.

From Fig. 20, it can be seen that the maximum equivalent stress of the internal rib of the deck structure occurs at the diagonal of the central column and the outer columns, where the vertical support is connected to the bottom of the deck. The vertical support transfers the load through the outer surface of the deck to the internal rib, with a maximum equivalent stress of 215.05 MPa.

As shown in Fig. 21, due to the influence of the static water pressure

Table 9
Design wave parameters.

Number	Hydrodynamic parameters	Period	Angle	Height	Phase	Response Peak
Design Wave 1	Transverse shear force	11.5 s	90°	17.30 m	-30.68°	1.58E+ 08
Design Wave 2	Longitudinal torque	7.5 s	90°	11.56 m	-25.61°	5.41E+ 09
Design Wave 3	Vertical bending moment	8.5 s	0°	13.99 m	-77.09°	1.29E+ 10
Design Wave 4	Lateral acceleration	10.5 s	90°	15.00 m	-81.06°	0.536
Design Wave 5	Longitudinal acceleration	10.5 s	30°	15.00 m	-81.06°	0.465
Design Wave 6	vertical acceleration	18 s	90°	17.30 m	-89.97°	0.418

Note: The peak response units of force, torque, and acceleration are N, N·m, and m/s^2.

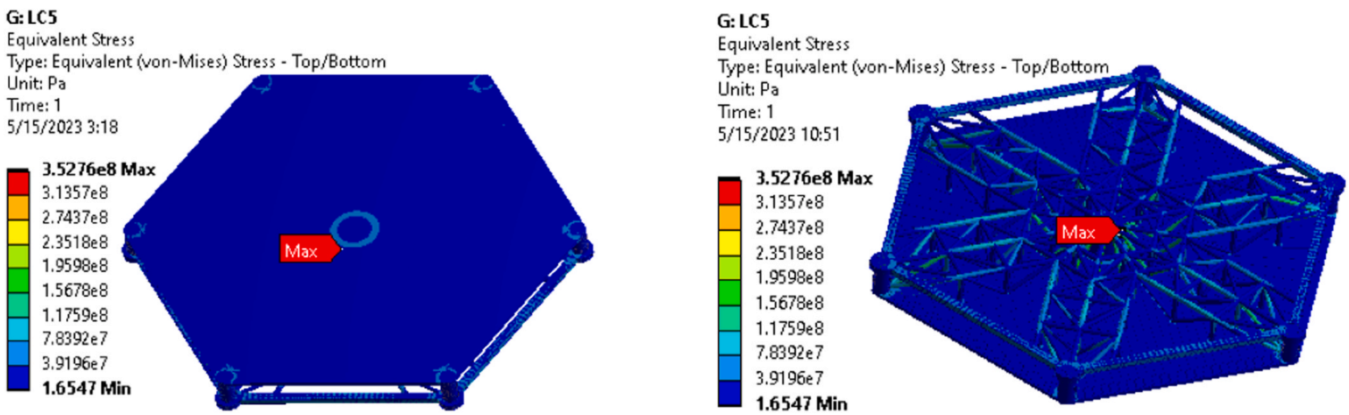

Fig. 17. Cloud Chart of Equivalent Forces on the Overall Structure of the Platform.

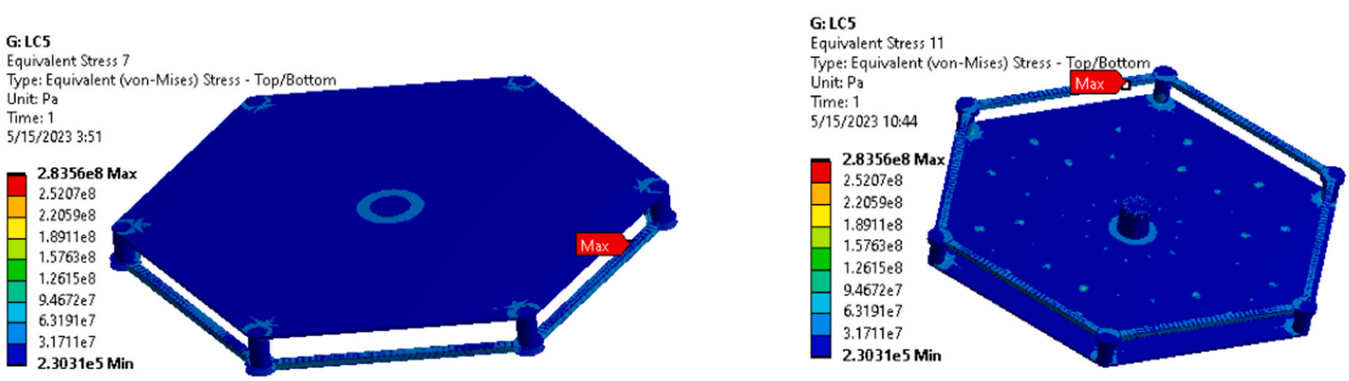

Fig. 18. Cloud diagram of equivalent force on the shell of the platform structure.

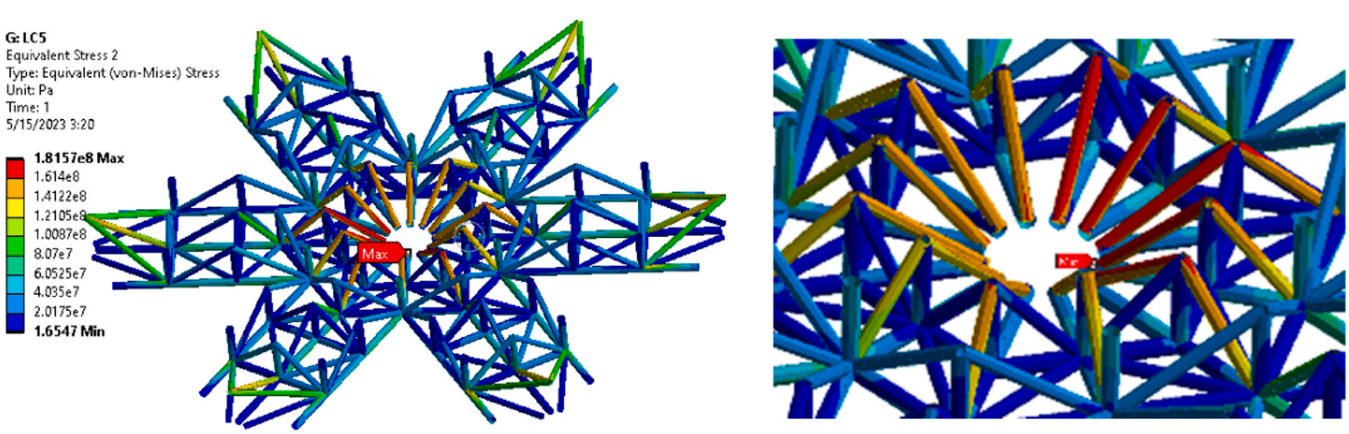

Fig. 19. Cloud chart of equivalent stress of transverse brace/slant support.

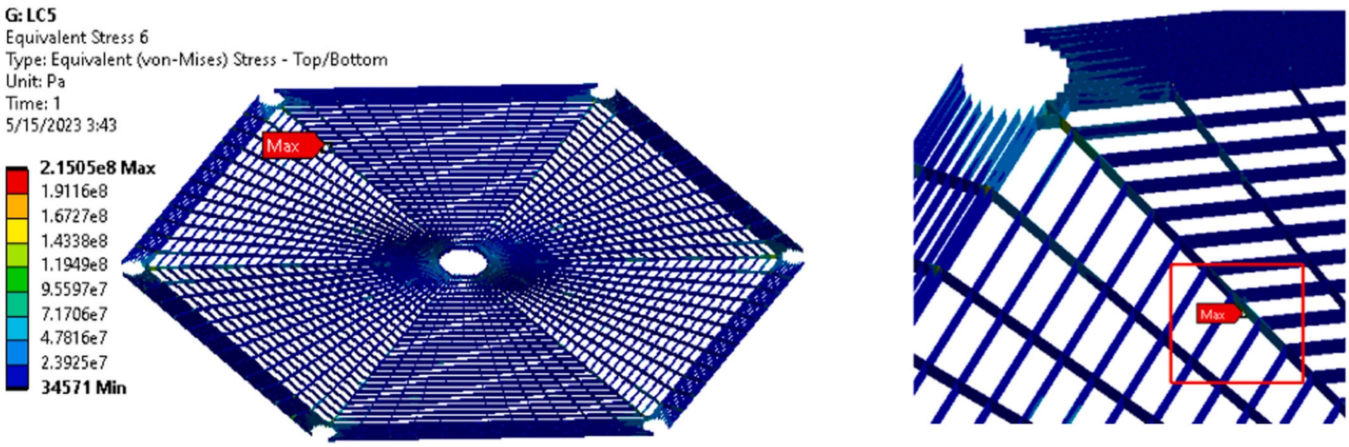

Fig. 20. Cloud chart of equivalent stress of internal structure of the deck.

and wave load of the lower ballast tank, the equivalent stress of the components below the shear surface is significantly higher than that of the upper components. The von Mises stress value at the junction of the pressurized water tank and the upper column is the highest 234.17 MPa. In addition, due to the randomness of wave loads, the stress distribution behavior of the six outer columns is slightly different.

It can be seen from Fig. 22 that the maximum Von Mises stress inside the central column is 352.76 MPa, which occurs at the junction of the lower vertical rib plate and the lower circumferential rib plate. This is the stress concentration phenomenon caused by the force transmission path formed by the connection between the central column, the transverse brace, and the slanted support.

The corresponding stress cloud maps of the internal structures of the six lower beams display an asymmetric distribution, as illustrated in Fig. 23. Among them, in the LC5 working condition, the maximum equivalent stress value of the internal structure of the lower crossbeam is 191.50 MPa, which occurs at the connection between the lower crossbeam and the transverse brace.

Figs. 17–23 show the equivalent stress cloud map of LC5 corresponding to the maximum stress value of the optimized platform, with the maximum equivalent stress value 352.76 MPa. Finally, Table 10 displays the maximum equivalent stress statistical values of each component of the platform under six operating load conditions.

5.4. Improve the strength verification results

The simulated results indicate that the maximum von Mises stress under all working conditions occurs at the circumferential rib plate at the lower part of the central column because this is the intersection between the outer surface of the lower part of the central column and the transverse support. It not only bears the action of wave loads but also receives axial loads from the transverse support, resulting in stress concentration.

According to the "Rules for Classification of Maritime Movements (2017)" [63], the yield failure criterion is used to perform strength testing at the floating platform structure. The allowable stress calculation formula for the components involved in structural analysis is as follows:

$$\sigma_{eq} \leq \frac{\sigma_s}{S} \tag{6}$$

In the formula $\sigma_s$is the yield strength of the material is 355 MPa, and S is the safety factor 1.11, hence, the equivalent stress of EH36 steel$\sigma_{eq}$is 320 MPa.

The maximum stress of the central column in working conditions LC1, LC3, and LC4 is slightly greater than the material allowable stress of 320 MPa, but all are within the allowable range of 5% safety limit, while the maximum equivalent stress of the central column in operating condition LC5 is 352.76 MPa, as shown in Fig. 22, exceeding the requirement of 10% safety limit.

To reduce the phenomenon of local stress concentration on the platform, it is possible to add rib plates, thicken plates, or change structural components within the structure. Due to the maximum equivalent stress of the selected working conditions occurring at the internal circumferential rib plate of the central column, this article

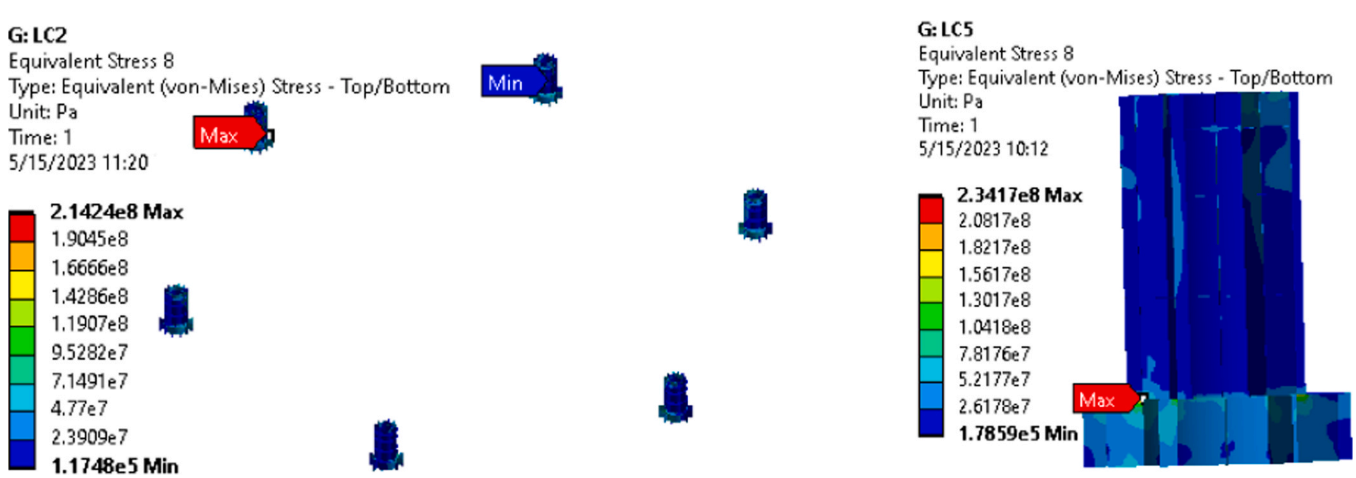

Fig. 21. Cloud chart of Equivalent forces on the internal structure of the outer column.

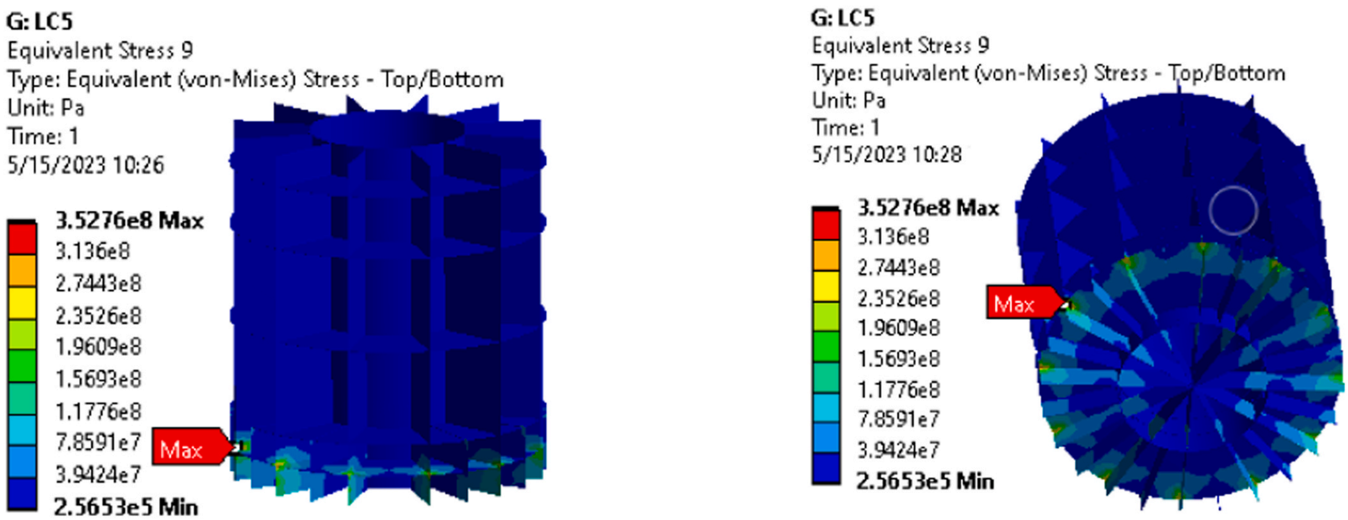

Fig. 22. Equivalent stress forces on the internal structure of the central column.

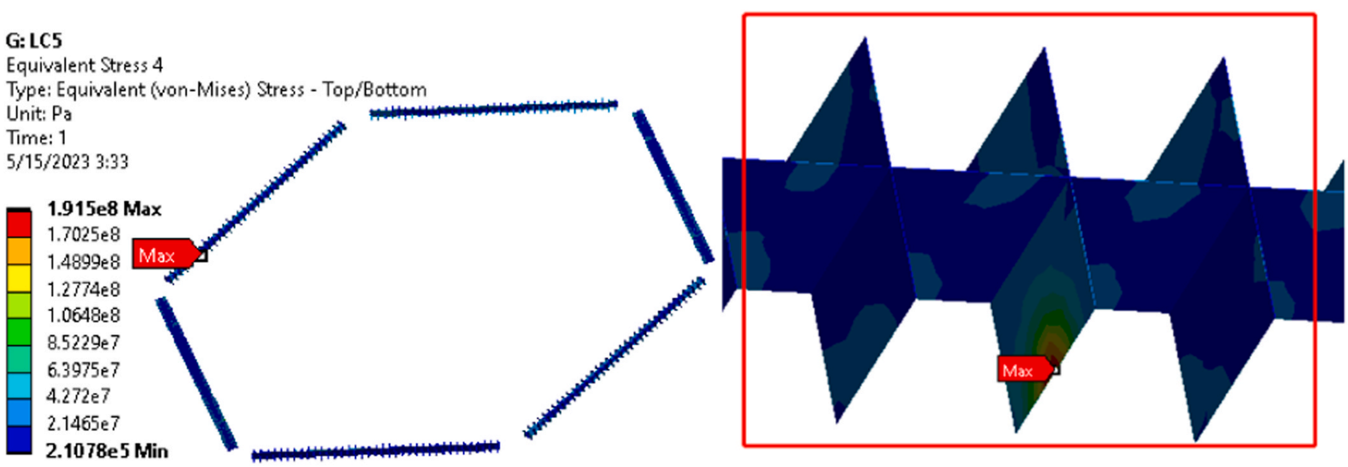

Fig. 23. Equivalent stress of internal structure of the lower cross bar.

Table 10
Maximum Equivalent (von Mises) Stress of main components of semi-submersible platform (Mpa).

LCs	Shell body	Transverse Braces	Internal Structure			
			Outer Column	Central Column	Crossbeam	Deck
LC1	315.23	184.52	255.27	321.47	207.99	208.18
LC2	239.74	176.37	214.24	303.54	153.40	210.65
LC3	251.83	180.39	241.71	325.19	153.89	209.87
LC4	281.99	189.54	231.64	321.38	190.99	222.77
LC5	283.56	181.57	234.17	352.76	191.50	215.05
LC6	269.21	183.14	223.48	316.04	171.33	224.46

adopts the following two schemes to reduce the local stress of the component:

1. Add two identical circumferential rib plates with a spacing of 1.5 m between the upper and lower circumferential rib plates with high stress range;
2. Increase the thickness of the circumferential rib plate at the stress concentration point to 40 mm.

Figs. 24 and 25 show the equivalent stress cloud diagrams of the internal structure of the central column reflecting the two schemes' outcomes. By adding circumferential ribs and increasing the thickness of the ribs, the maximum equivalent stress has been significantly reduced. Among them, the maximum equivalent stress of scheme 1 is 303.19 MPa, with a decrease of approximately 14%;.

The maximum equivalent stress of scheme 2 is 312.72 MPa, with a decrease of approximately 11%, which meets the limit requirements for allowable stress. By adding circumferential ribs, the range of high stress areas can be dispersed, but it cannot effectively solve the problem of stress concentration caused by the force transmission. Due to the small difference in stress reduction between the two schemes and considering factors such as platform cost, Scheme 2 is adopted to increase the thickness of the circumferential rib plate to reduce the equivalent stress of the entire platform. Table 11 presents the statistical results of the maximum equivalent stress values of the platform under various working conditions after the scheme 2 execution. Results show that this scheme effectively reduces the maximum stress of the columns under various operating conditions. The technical roadmap of this paper is shown in Fig. 26 respectively.

6. Conclusion

Aiming at the integrated development and utilization of energy in the deep ocean, this study proposes a conceptual design of a

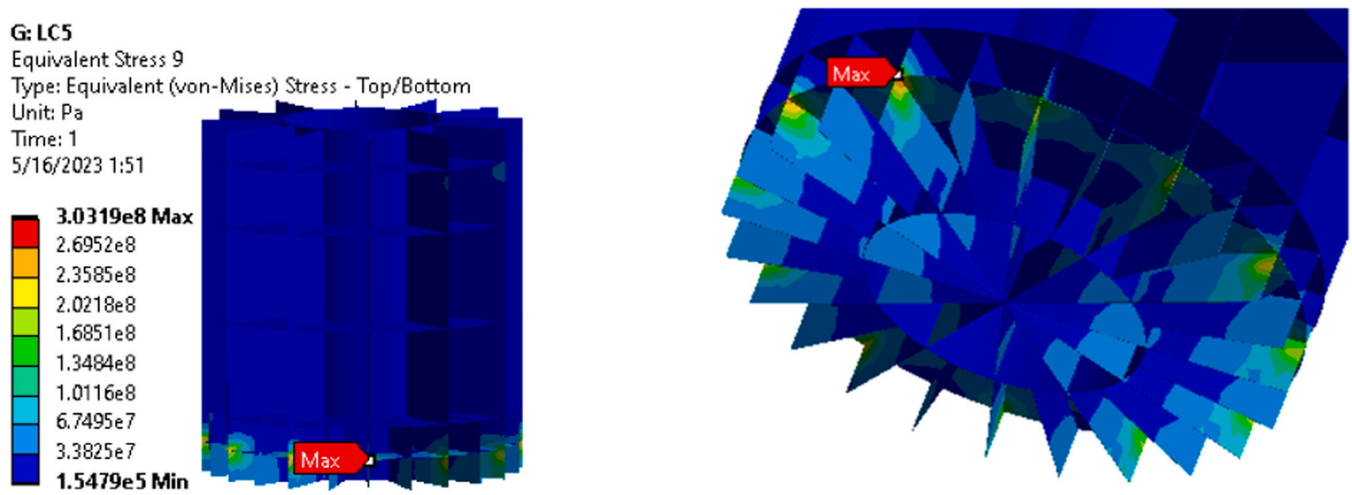

Fig. 24. Equivalent (von Mises) stress at the internal structure of the central column (Scheme 1).

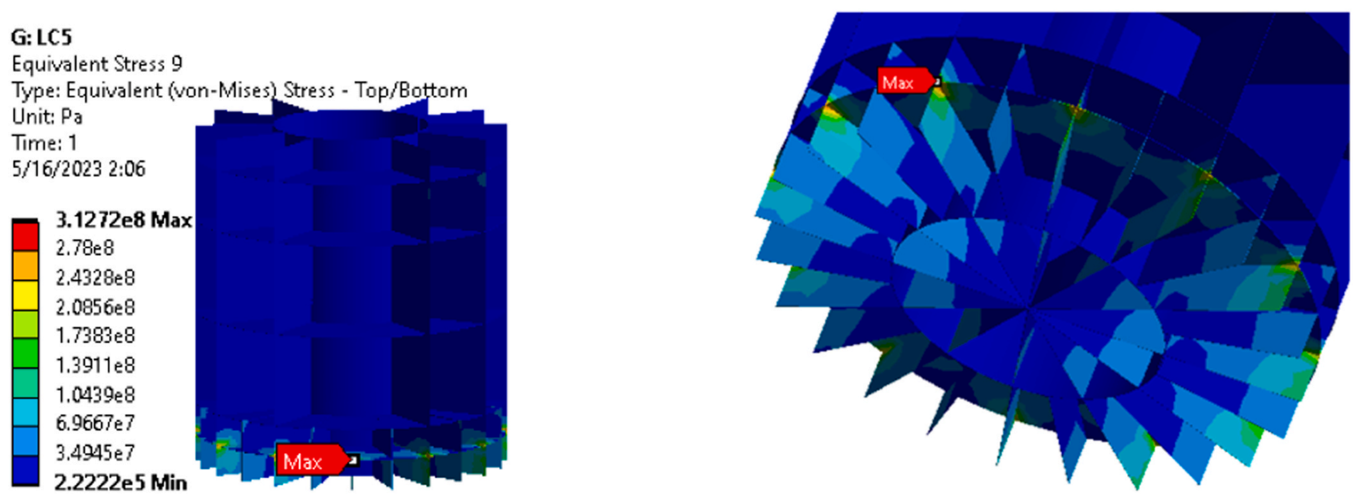

Fig. 25. Equivalent (von Mises) stress at the internal structure of the central column (Scheme 2).

Table 11
Maximum equivalent stress of main components of platform (Improved) (MPa).

LCs	Shell body	Transverse Brace	Internal Structure			
			Outer Column	Central Column	Crossbeam	Deck
LC1	315.20	184.97	255.25	285.76	207.98	208.24
LC2	240.04	176.57	214.23	270.13	153.38	210.71
LC3	251.97	180.59	241.70	307.24	153.89	209.90
LC4	281.94	189.74	231.64	275.68	190.97	222.84
LC5	283.35	181.78	234.18	312.72	191.48	215.12
LC6	269.13	183.24	223.48	281.45	171.29	224.52

multifunctional floating optimized platform structure, which integrates three DTU 10 MW wind turbines, a 4.4 MW wave energy device and an 11.4 MW solar energy generation devices to achieve the goal of wind-solar-wave power generation.

In addition, calculates the wave load at the optimized floating platform through the deterministic design wave method according to the relevant specifications of DNV and China Classification Society for column stabilized platforms, and uses the ANSYS workbench to analyse the strength verification by mapping the wave load in the form of surface load combined with other loads, and draws the following conclusions:

1. Based on the environmental conditions of the South China Sea, the variable density-based topology optimization approach is carried out to find the optimal material distribution inside the proposed multi-functional platform to accomplish the lightweight design and maximize the stiffness. The topological configuration of cells with a density between 0.6-1 has a clearer force transfer path. The truss structure is used to re-design the topological optimized results, accomplish the lightweight design and maximize the stiffness to improve the overall stability.
2. By using the Hydrodynamic Diffraction module, the required hydrodynamic characteristic parameters for the design wave method are determined, and the amplitude frequency function of the hydrodynamic characteristic parameters for the response of the proposed floating platform is calculated in the frequency domain. According to the amplitude transfer function of each section load, it can be seen that the floating platform is mainly affected by lateral acceleration force, bending moment, and torque.
3. Based on the design wave method and static analysis, the strength of the proposed multifunctional optimized platform is checked, and the maximum von Mises stress of each component is obtained. From the stress results, it can be seen that the von Mises stress of the component is less than the allowable stress of high-strength steel EH36 of 320 MPa. The weak area of the platform stress mainly occurs in the connection between components, including the transverse brace and

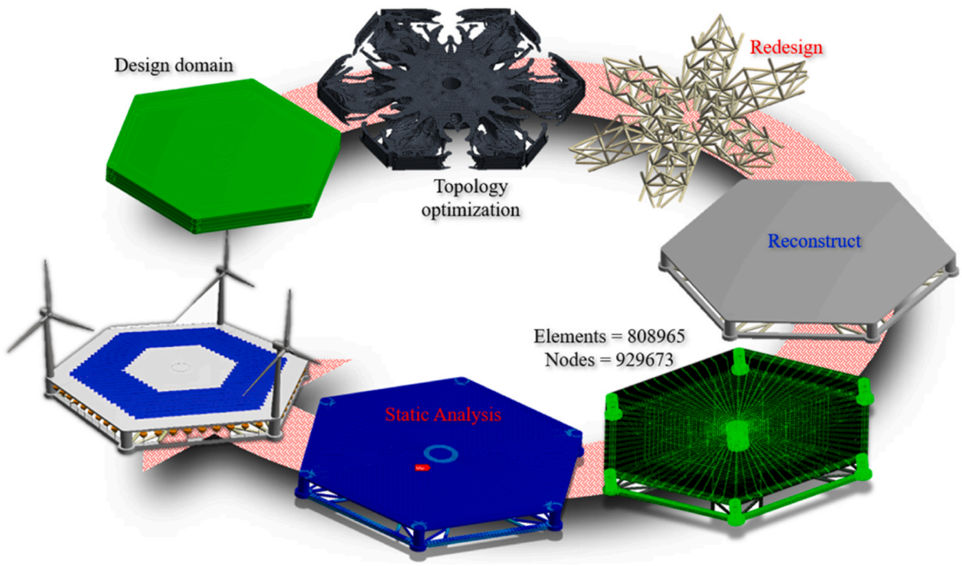

Fig. 26. The technical roadmap.

the central column, the slant support/transverse brace and the bottom of the deck, the deck and the central/outer column intersection between the slant support/cross beam and lower cross beam.

4. The maximum stress of the proposed multifunctional floating optimized platform structure occurs under the LC5 load combination condition, with a maximum stress value of 352.76 MPa, which exceeds approximately 10% of the allowable stress safety limit. By adding circumferential rib plates and increasing the thickness of local rib plates, the maximum equivalent stress can meet the safety limit requirements of allowable stress. The overall stress reduction of the two improvement schemes is 14% and 11%. Considering factors such as cost, the internal structure of the central column was improved by increasing the thickness of local rib plates. The stress results of all calculation conditions in the improved model were lower than the allowable stress.

Finally, the conceptual proposed design model of the large multifunctional floating optimized platform was obtained to carry out the subsequent research work of strength verification, and stability analysis of the platform.

CRediT authorship contribution statement

Nouman Saeed: Conceptualization, Validation, Writing – original draft. **Jingliang Gong:** Conceptualization, Validation. **Yuejia Wan:** Formal analysis, Validation. **Kai Long:** Data curation, Investigation. **Ayesha Saeed:** Data curation, Investigation. **Liu Mei:** Formal analysis, Visualization. **Chen Xiong:** Formal analysis, Visualization. **Wujian Long:** Writing – original draft. **Haijun Zhou:** Writing – review & editing. **lixiao li:** Conceptualization, Supervision, Writing – review & editing.

Declaration of Competing Interest

The authors state that they do not have any known conflicting financial interests or connections that may seem to have influenced the work reported in this study.

Data Availability

Data will be made available on request.

Acknowledgements

The support for this research has been provided by the National Natural Science Foundation of China (Grant No. 52178491, 51778373), the Natural Science Foundation of Guangdong Province (Grant No. 2022A1515011499 and 2021A1515011769), the Natural Science Foundation of Shenzhen (Grant No. JCYJ 20210324093809023) and Shenzhen Key Laboratory of Structure Safety and Health Monitoring of Marine Infrastructures (Grant No. ZDSYS20201020162400001) Shenzhen Science and Technology Program (Grant No. KQTD 2020 0820 1130 04005) are gratefully acknowledged.

References

[1] Lorente DB, Mohammed KS, Cifuentes-Faura J, Shahzad U. Dynamic connectedness among climate change index, green financial assets and renewable energy markets: novel evidence from sustainable development perspective. Renew Energy 2023;204:94–105.
[2] Cheng Z, Kai Z, Zhu S. Does green finance regulation improve renewable energy utilization? Evidence from energy consumption efficiency. Renew Energy 2023;208:63–75.
[3] Hoogwijk M, De Vries B, Turkenburg W. Assessment of the global and regional geographical, technical and economic potential of onshore wind energy. Energy Economics 2004;26(5):889–919.
[4] Yang HS, Tongphong W, Ali A, Lee YH. Comparison of different fidelity hydrodynamic-aerodynamic coupled simulation code on the 10 MW semi-submersible type floating offshore wind turbine. Ocean Eng 2023;281:114736.
[5] Luo Y, Qian F, Sun H, Wang X, Chen A, Zuo L. Rigid-flexible coupling multi-body dynamics modeling of a semi-submersible floating offshore wind turbine. Ocean Eng 2023:114648.
[6] Ning Y, Wang L, Yu X, Li J. Recent development in the decarbonization of marine and offshore engineering systems. Ocean Eng 2023;280:114883.
[7] Han D, Li X, Wang W, Su X. Dynamic modeling and vibration control of barge offshore wind turbine using tuned liquid column damper in floating platform. Ocean Eng 2023;276:114299.
[8] Yan X, Chen C, Yin G, Ong MC, Ma Y, Fan T. Numerical investigations on nonlinear effects of catenary mooring systems for a 10-MW FOWT in shallow water. Ocean Eng 2023;276:114207.
[9] Ferri G, Marino E, Bruschi N, Borri C. Platform and mooring system optimization of a 10 MW semisubmersible offshore wind turbine. Renew Energy 2022;182:1152–70.
[10] Ferri G, Marino E. Site-specific optimizations of a 10 MW floating offshore wind turbine for the Mediterranean Sea. Renew Energy 2023;202:921–41.
[11] Shi W, Hu L, Lin Z, Zhang L, Wu J, Chai W. Short-term motion prediction of floating offshore wind turbine based on muti-input LSTM neural network. Ocean Eng 2023;280:114558.
[12] Ferri G, Marino E, Borri C. Optimal dimensions of a semisubmersible floating platform for a 10 MW wind turbine. Energies 2020;13(*12*):3092.
[13] Centeno-Telleria M, Aizpurua JI, Penalba M. Impact of accessibility on O&M of floating offshore wind turbines: sensitivity of the deployment site. Trends Renew Energ Offshore 2023:847–55.

[14] Saeed N, Li L, Long K, Zhou H, Saeed A, Yang X, et al. A Quadratic Approximation for Volume Minimization Topology Optimization. Structures, Vol. 53. Elsevier; 2023. p. 1341–8.
[15] Saeed N, Long K, Li L, Saeed A, Zhang C, Cheng Z. An augmented Lagrangian method for multiple nodal displacement-constrained topology optimization. Eng Optim 2022:1–15.
[16] Chen Z, Long K, Wen P, Nouman S. Fatigue-resistance topology optimization of continuum structure by penalizing the cumulative fatigue damage. Adv Eng Softw 2020;150:102924.
[17] Long K, Yang X, Saeed N, Tian R, Wen P, Wang X. Topology optimization of transient problem with maximum dynamic response constraint using SOAR scheme. Front Mech Eng 2021;16(3):593–606.
[18] Long K, Chen Z, Zhang C, Yang X, Saeed N. An aggregation-free local volume fraction formulation for topological design of porous structure. Materials 2021;14(19):5726.
[19] Long K, Yang X, Saeed N, Chen Z, Xie YM. Topological design of microstructures of materials containing multiple phases of distinct poisson's ratios. Comput Model Eng Sci 2021;126(1):293–310.
[20] Bendsøe MP, Kikuchi N. Generating optimal topologies in structural design using a homogenization method. Comput Methods Appl Mech Eng 1988;71(2):197–224.
[21] Sigmund O. A 99 line topology optimization code written in Matlab. Struct Multidiscip Optim 2001;21:120–7.
[22] Andreassen E, Clausen A, Schevenels M, Lazarov BS, Sigmund O. Efficient topology optimization in MATLAB using 88 lines of code. Struct Multidiscip Optim 2011;43:1–16.
[23] Sigmund O, Petersson J. Numerical instabilities in topology optimization: a survey on procedures dealing with checkerboards, mesh-dependencies and local minima. Struct Optim 1998;16:68–75.
[24] Sigmund O, Maute K. Topology optimization approaches: a comparative review. Struct Multidiscip Optim 2013;48(6):1031–55.
[25] Huang X, Xie YM. A further review of ESO type methods for topology optimization. Struct Multidiscip Optim 2010;41:671–83.
[26] Li L, Liu C, Zhang W, Du Z, Guo X. Combined model-based topology optimization of stiffened plate structures via MMC approach. Int J Mech Sci 2021;208:106682.
[27] Zhu JH, Zhang WH, Xia L. Topology optimization in aircraft and aerospace structures design. Arch Comput Methods Eng 2016;23:595–622.
[28] Munk DJ, Auld DJ, Steven GP, Vio GA. On the benefits of applying topology optimization to structural design of aircraft components. Struct Multidiscip Optim 2019;60:1245–66.
[29] Zhang Y, Shan Y, Liu X, He T. An integrated multi-objective topology optimization method for automobile wheels made of lightweight materials. Struct Multidiscip Optim 2021;64:1585–605.
[30] Zhu B, Zhang X, Zhang H, Liang J, Zang H, Li H, et al. Design of compliant mechanisms using continuum topology optimization: a review. Mech Mach Theory 2020;143:103622.
[31] Mitchell, S.L., 2016. Topology optimization of silicon anode structures for lithium-ion battery applications. California Institute of Technology.
[32] Long K, Du X, Xu S, Xie YM. Maximizing the effective Young's modulus of a composite material by exploiting the Poisson effect. Compos Struct 2016;153:593–600.
[33] Sigmund O, Maute K. Topology optimization approaches: A comparative review. Struct Multidiscip Optim 2013;48(6):1031–55.
[34] Lu F, Long K, Zhang C, Zhang J, Tao T. A novel design of the offshore wind turbine tripod structure using topology optimization methodology. Ocean Eng 2023;280:114607.
[35] Zhang C, Long K, Zhang J, Lu F, Bai X, Jia J. A topology optimization methodology for the offshore wind turbine jacket structure in the concept phase. Ocean Eng 2022;266:112974.
[36] Lu F, Long K, Diaeldin Y, Saeed A, Zhang J, Tao T. A time-domain fatigue damage assessment approach for the tripod structure of offshore wind turbines. Sustain Energy Technol Assess 2023;60:103450.
[37] Zhang P, Li J, Gan Y, Zhang J, Qi X, Le C, et al. Bearing capacity and load transfer of brace topological in offshore wind turbine jacket structure. Ocean Eng 2020;199:107037.
[38] Tian X, Wang Z, Liu D, Liu G, Deng W, Xie Y, et al. Jack-up platform leg optimization by topology optimization algorithm-BESO. Ocean Eng 2022;257:111633.
[39] Tian X, Sun X, Liu G, Deng W, Wang H, Li Z, et al. Optimization design of the jacket support structure for offshore wind turbine using topology optimization method. Ocean Eng 2022;243:110084.
[40] Karimi M, Hall M, Buckham B, Crawford C. A multi-objective design optimization approach for floating offshore wind turbine support structures. J Ocean Eng Mar Energy 2017;3:69–87.
[41] Karimi M, Buckham B, Crawford C. A fully coupled frequency domain model for floating offshore wind turbines. J Ocean Eng Mar Energy 2019;5:135–58.
[42] Yang H, Zhu Y, Lu Q, Zhang J. Dynamic reliability based design optimization of the tripod sub-structure of offshore wind turbines. Renew Energy 2015;78:16–25.
[43] Gentils T, Wang L, Kolios A. Integrated structural optimisation of offshore wind turbine support structures based on finite element analysis and genetic algorithm. Appl Energy 2017;199:187–204.
[44] Motlagh AA, Shabakhty N, Kaveh A. Design optimization of jacket offshore platform considering fatigue damage using genetic algorithm. Ocean Eng 2021;227:108869.
[45] Song J, Chen J, Wu Y, Li L. Topology optimization-driven design for offshore composite wind turbine blades. J Mar Sci Eng 2022;10(10):1487.
[46] Tian X, Wang Q, Liu G, Liu Y, Xie Y, Deng W. Topology optimization design for offshore platform jacket structure. Appl Ocean Res 2019;84:38–50.
[47] Bak C, Zahle F, Bitsche R, Kim T, Yde A, Henriksen LC, et al. The DTU 10-MW reference wind turbine. Dan Wind Power Res 2013:*2013*.
[48] Tao T, Long K, Yang T, Liu S, Yang Y, Guo X, et al. Quantitative assessment on fatigue damage induced by wake effect and yaw misalignment for floating offshore wind turbines. Ocean Eng 2023;288:116004.
[49] Tian L, Zhu W, Shen W, Song Y, Zhao N. Prediction of multi-wake problems using an improved Jensen wake model. Renew Energy 2017;102:457–69.
[50] Shakoor R, Hassan MY, Raheem A, Wu YK. Wake effect modeling: a review of wind farm layout optimization using Jensen′ s model. Renew Sustain Energy Rev 2016;58:1048–59.
[51] Saeidtehrani S, Fazeres-Ferradosa T, Rosa-Santos P, Taveira-Pinto F. Review on floating wave-wind energy converter plants: Nonlinear dynamic assessment tools. Sustain Energy Technol Assess 2022;54:102753.
[52] Bose, B.K., 2020. Power electronics and motor drives: advances and trends.
[53] Lee YS, Yang MS, Kim HS, Kim JH. A study on the free vibration of the joined cylindrical–spherical shell structures. Comput Struct 2002;80(27-30):2405–14.
[54] Zhou BZ, Hu JJ, Sun K, Liu Y, Collu M. Motion response and energy conversion performance of a heaving point absorber wave energy converter. Front Energy Res 2020;8:553295.
[55] Sheng S, Wang K, Lin H, Zhang Y, You Y, Wang Z, et al. Model research and open sea tests of 100 kW wave energy convertor Sharp Eagle Wanshan. Renew Energy 2017;113:587–95.
[56] Fahrenbruch A, Bube R. Fundamentals of Solar Cells: Photovoltaic Solar Energy Conversion. Elsevier; 2012.
[57] Ball JM, Lee MM, Hey A, Snaith HJ. Low-temperature processed meso-superstructured to thin-film perovskite solar cells. Energy Environ Sci 2013;6(6):1739–43.
[58] Portella KF, Paludo R, Carneiro GL, Bernardo JWY, Sieciechowicz MSF, Bragança MDOGP, Fr AC. Feasibility and environmental sustainability of a 103.5 kWp floating photovoltaic electrical system with a case study in a hydroelectric power plant, Santa Clara Hpp, Located in the South of Brazil Region. Int J Adv Eng Res Sci 2018;5(6):264141.
[59] DNV, G., 2016. Design of offshore steel structures, general (LRFD method). *DNVGL-OS-C101*.
[60] Fisher A, Thomson J, Schwendeman M. Rapid deterministic wave prediction using a sparse array of buoys. Ocean Eng 2021;228:108871.
[61] Xu WH, Pang T, Yan SM, Zhai LB, Kang YW, Zhang SH. Prediction of collapse pressure of submarine pipelines in a wide range of diameter-thickness ratio. China Ocean Eng 2022;36(4):565–74.
[62] Wang, A., Basu, P., Loo, B.T., Sokolsky, O., 2009. Declarative network verification. In Practical Aspects of Declarative Languages: 11th International Symposium, PADL 2009, Savannah, GA, USA, January 19–20, 2009. Proceedings 11 (pp. 61–75). Springer Berlin Heidelberg.
[63] Maritime, B.V., 2017. Rules on materials and welding for the classification of marine units'.